

# Electronic structure studies of $\text{BaFe}_2\text{As}_2$ by angle-resolved photoemission spectroscopy

J. Fink,<sup>1,2</sup> S. Thirupathaiah,<sup>1</sup> R. Ovsyannikov,<sup>1</sup> H.A. Dürr,<sup>1</sup> R. Follath,<sup>1</sup> Y. Huang,<sup>3</sup> S. de Jong,<sup>3</sup> M.S. Golden,<sup>3</sup> Yu-Zhong Zhang,<sup>4</sup> H.O. Jeschke,<sup>4</sup> R. Valentí,<sup>4</sup> C. Felser,<sup>5</sup> S. Dastjani Farahani,<sup>5</sup> M. Rotter,<sup>6</sup> D. Johrendt,<sup>6</sup>

<sup>1</sup> Helmholtz-Zentrum Berlin, Albert-Einstein-Strasse 15, 12489 Berlin, Germany

<sup>2</sup> Leibniz-Institute for Solid State and Materials Research Dresden, P.O.Box 270116, D-01171 Dresden, Germany

<sup>3</sup> Van der Waals-Zeeman Institute, University of Amsterdam, NL-1018XE Amsterdam, The Netherlands

<sup>4</sup> Inst. für Theor. Physik, Goethe-Universität, Max-von-Laue-Straße 1, 60438 Frankfurt, Germany

<sup>5</sup> Inst. für Anorg. Chemie und Anal. Chemie, Johannes Gutenberg-Universität, 55099 Mainz, Germany

<sup>6</sup> Department Chemie und Biochemie, Ludwig-Maximilians-Universität München, 81377 München, Germany

(Dated: February 12, 2022)

We report high resolution angle-resolved photoemission spectroscopy (ARPES) studies of the electronic structure of  $\text{BaFe}_2\text{As}_2$ , which is one of the parent compounds of the Fe-pnictide superconductors. ARPES measurements have been performed at 20 K and 300 K, corresponding to the orthorhombic antiferromagnetic phase and the tetragonal paramagnetic phase, respectively. Photon energies between 30 and 175 eV and polarizations parallel and perpendicular to the scattering plane have been used. Measurements of the Fermi surface yield two hole pockets at the  $\Gamma$ -point and an electron pocket at each of the X-points. The topology of the pockets has been concluded from the dispersion of the spectral weight as a function of binding energy. Changes in the spectral weight at the Fermi level upon variation of the polarization of the incident photons yield important information on the orbital character of the states near the Fermi level. No differences in the electronic structure between 20 and 300 K could be resolved. The results are compared with density functional theory band structure calculations for the tetragonal paramagnetic phase.

PACS numbers: 74.70.-b, 74.25.Jb, 79.60.-i, 71.20.-b

## I. INTRODUCTION

The discovery of high superconducting transition temperatures up to 55 K in iron oxypnictides<sup>1,2,3</sup> has brought a lot of attention to compounds containing FeAs layers. Soon thereafter high superconducting transition temperatures were also discovered in the structurally related, non-oxide material  $\text{Ba}_{1-x}\text{K}_x\text{Fe}_2\text{As}_2$ .<sup>4</sup> Similar to the cuprate superconductors, the parent compounds of the FeAs-based superconductors have to be doped or, differently from the cuprates, have to be set under pressure to yield superconductivity. A further difference between the cuprates and iron pnictides is that the parent compounds in the latter are not antiferromagnetic Mott-Hubbard insulators but metals with an antiferromagnetic ordering. Nevertheless superconductivity appears in doped iron pnictides in which antiferromagnetic ordering is suppressed. There have been many discussions about the relation of a quantum critical point due to magnetic order and high- $T_c$  superconductivity. In the iron pnictides the antiferromagnetic ordering is supposed to occur by a nesting of hole pockets at the center of the Brillouin zone and electron pockets at the zone corner (X-point in a primitive tetragonal zone).<sup>5</sup> The Brillouin zone for  $\text{BaFe}_2\text{As}_2$  is presented in Fig. 1. This nesting scenario may be also important for the pairing mechanism in these compounds. In order to understand the electronic structure of the new high- $T_c$  superconductors it is therefore important to study the electronic structure of the parent compounds.

In this contribution we present the study of the electronic structure of the parent compound of the super-

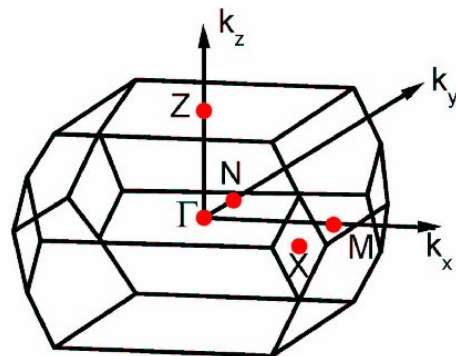


Figure 1: (color online) Brillouin zone of  $\text{BaFe}_2\text{As}_2$  in the tetragonal phase. The presented ARPES data are focused around the  $\Gamma$  and around the X-point.

conductors  $\text{BaFe}_2\text{As}_2$  under pressure,  $\text{Ba}_{1-x}\text{K}_x\text{Fe}_2\text{As}_2$ , and  $\text{BaFe}_{2-x}\text{Co}_x\text{As}_2$  using high resolution angle-resolved photoemission spectroscopy (ARPES). Previously other groups have used ARPES to study the electronic structure of these parent compounds and their related superconductors.<sup>6,7,8,9,10,11,12,13,14,15,16</sup> In the present study we focus on the possible differences between the electronic structure in the paramagnetic tetragonal state and in the antiferromagnetic orthorhombic state of  $\text{BaFe}_2\text{As}_2$  by performing temperature dependent measurements. This is an interesting topic since the sudden decrease of the resistivity below the Neel temperature seen in transport data may indicate that a change occurs in the electronic structure. A change of the band structure is also predicted from density functional theory (DFT) calculations.<sup>17,18,19,20</sup> Furthermore, we have

performed ARPES experiments with different polarizations of the photons in order to obtain information about the orbital character of the bands close to the Fermi level. In addition, using the variable photon energies available from the synchrotron radiation source, we have obtained information relevant to the  $k_z$  values sampled in the measurements, and also are able to make an initial examination of the dispersion of the bands perpendicular to the FeAs planes. The experimental results are compared with our DFT band structure calculations and with similar work in the literature on doped and undoped  $\text{BaFe}_2\text{As}_2$ .<sup>9,17,18,19,21</sup>

## II. EXPERIMENTAL DETAILS

Single crystals of  $\text{BaFe}_2\text{As}_2$  were grown out of a Sn flux in Amsterdam and München, using conventional high temperature solution growth techniques. Elemental analysis of the former was performed using wavelength dispersive X-ray spectroscopy (WDS). Further elemental analysis was obtained from X-ray induced photoemission spectroscopy on the core levels.<sup>22</sup> Both methods yielded a Sn contamination of the crystal of approximately 1.6 atomic %. According to a recent study of  $\text{BaFe}_2\text{As}_2$  single crystals, such a Sn contamination leads to a reduction of the structural transition temperature from the tetragonal to the orthorhombic phase and also to a reduction of the transition between the paramagnetic and the antiferromagnetic phase.<sup>23</sup> Polycrystalline Sn-free samples show transition temperatures close to 140 K. For the Amsterdam crystals a transition temperature of  $\approx 65$  K was deduced from resistivity measurements. Therefore they are termed BFA65K. For the München crystals a structural transition and a Neel temperature at  $\approx 100$  K are derived from neutron scattering data<sup>24</sup> and therefore they are termed BFA100K. The higher transition temperature of this crystal when compared to the BFA65K crystals indicates a lower Sn content.

The ARPES experiments were carried out at the BESSY synchrotron radiation facility using the U125/1-PGM beam line and the "1<sup>3</sup>-ARPES" end station provided with a SCIENTA R4000 analyzer. Spectra were taken with various photon energies ranging from  $h\nu = 30$  to 175 eV. The total energy resolution ranged from 10 meV (FWHM) at photon energies  $h\nu = 30$  eV to 20 meV at  $h\nu = 175$  eV. The angular resolution was  $0.2^\circ$  along the slit of the analyzer and  $0.3^\circ$  perpendicular to it. The experimental geometry is depicted in Fig. 2 and is also described in more detail in a previous paper.<sup>25</sup> In this geometry the scattering plane, as defined by the direction of the incoming photons and the trajectory of the outgoing photoelectrons, is nearly horizontal for  $k_y = 0$ , i.e., for photoelectrons traveling to the center of the entrance slit of the analyzer.

The present ARPES study was mainly focused to two regions in the Brillouin zone: round the zone center (the  $\Gamma = (0,0,0)$  and  $Z = \frac{\pi}{c}(0,0,1)$  points) and the zone corner

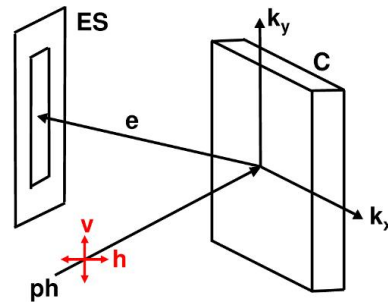


Figure 2: (color online) measuring geometry for the ARPES data taken near the  $\Gamma$ -point. The entrance slit (ES) of the analyzer, the crystal (C), the vertical (v) and the horizontal (h) linear polarization of the incoming photons (ph), and the trajectory of the outgoing photoelectrons (e) are shown. The direction of the photons and the photoelectrons define the scattering plane. This scattering plane is almost horizontal for photoelectrons traveling to the center of the entrance slit ( $k_y=0$ ).

( $X = \frac{\pi}{a}(1,1,0)$  point), as illustrated in Fig. 1, where  $a$  and  $c$  are the tetragonal lattice constants for  $\text{BaFe}_2\text{As}_2$  along  $x$  and the  $z$ -axis, respectively. For recording data at the  $\Gamma$ -point we oriented the crystal in such a way that the  $k_x(k_y)$  direction was parallel to the  $\Gamma$ -M(N) direction, where  $M = \frac{\pi}{a}(1,0,0)$ ,  $N = \frac{\pi}{a}(0,1,0)$ . In this way the  $\Gamma$ MZ-mirror plane of the crystal is in the scattering plane. Using a helical undulator, the linear polarization of the incoming synchrotron radiation could be changed from the horizontal direction to the vertical direction. Due to symmetry selection rules within the matrix elements governing photoemission, the experimental intensities are strongly affected by the orientation of the polarization of the photons relative to the scattering plane.<sup>26</sup> For  $k_y = 0$ , i.e., for photoelectrons traveling to the center of the exit slit, vertical (horizontal) polarization means that the electric field vector is essentially perpendicular (parallel) to the scattering plane, yielding the label s(p) for the two polarization geometries. We emphasize that due to the finite size of the vertically aligned entrance slit this only holds for the center of this slit. Orienting a mirror plane of the crystal into the scattering plane and performing polarization dependent ARPES experiments, important information on the parity of orbitals relative to the mirror plane can be obtained. Since the final state is even with respect to reflection in the mirror plane, the matrix element and thus the intensity should vanish when the product of the dipole operator and the initial state is odd. This means that the intensity from initial state orbitals having odd(even) parity relative to the mirror plane should disappear for parallel(perpendicular) photon polarization (or p[s] polarizations) relative to the mirror plane.

For recording data at the X-point the crystal was rotated around its normal by  $45^\circ$ . The horizontal (vertical) direction, which we now term  $k_{x'}(k_{y'})$ , is parallel to the  $\Gamma$ -X(Y) direction where  $Y = \frac{\pi}{a}(-1,1,0)$ . In this way the

$\Gamma$ XZ-mirror plane lies in the scattering plane for  $k_y = 0$ .

Finally, for exploring the photon energy dependence of the data and for elucidating the  $k_z$  values sampled under our experimental conditions ( $k_z$  values near the  $\Gamma$ -point, parallel to  $\Gamma$ -Z, we recorded the kinetic energy of the photoelectrons in nearly normal emission for various  $k_y$  values (along the  $\Gamma$ -N direction) as a function of the photon energy.

Samples were mounted on a high-precision cryomanipulator and cleaved in situ at room temperature in an ultrahigh-vacuum chamber with a base pressure of  $10^{-10}$  mbar.

Most of the data presented here were taken from the larger BFA65K crystals. In some cases (marked in the figure captions), we also present data from the much smaller BFA100K crystals.

### III. BAND STRUCTURE CALCULATIONS

For comparison with ARPES data we calculated the electronic band structure of tetragonal paramagnetic  $\text{BaFe}_2\text{As}_2$  within the DFT in the generalized gradient approximation (GGA)<sup>27</sup> using the full-potential linearized augmented plane-wave code WIEN2k.<sup>28</sup> We considered a  $k$  mesh of  $40 \times 40 \times 40$  in the irreducible Brillouin zone and an accuracy benchmark for the LAPW (Linear augmented plane wave basis) of  $\text{Rk}_{\text{max}} = 7$ . We performed calculations (i) by fixing the As position to the experimental value<sup>29</sup> (ii) by fully relaxing the lattice parameters as well as the internal As coordinate within spin-polarized GGA.<sup>30</sup> Good agreement with ARPES is only obtained when the As position is kept as given by the neutron diffraction data,<sup>29</sup> as presented in this work or by performing GGA calculations on the optimized structure with tetragonalization.<sup>30</sup>

In Fig. 3 we show the calculated band structure for  $\text{BaFe}_2\text{As}_2$  close to the Fermi level along the  $\Gamma$ -M and the  $\Gamma$ -X direction. In Fig. 4 and Fig. 5 we depict calculated constant energy contours for various binding energies close to the  $\Gamma$ - and the X-point, respectively.

### IV. RESULTS

In Fig. 6 we show ARPES data of  $\text{BaFe}_2\text{As}_2$  near the  $\Gamma$ -point recorded at a temperature of 20 K using photons polarized parallel to the vertical direction, i.e., s-polarization for a horizontal scattering plane. In Fig. 6 (a) we depict momentum distribution maps for various binding energies. We remark here that we also present data for energies above the Fermi level since due to thermal excitation, states above  $E_F$  can be populated and thus can be detected by ARPES. In the momentum distribution map for  $E = E_F$  an almost circular Fermi surface is realized. The increasing diameter with increasing binding energy indicates clearly that this Fermi surface is caused by a hole pocket centered at the  $\Gamma$ -point. A Fermi

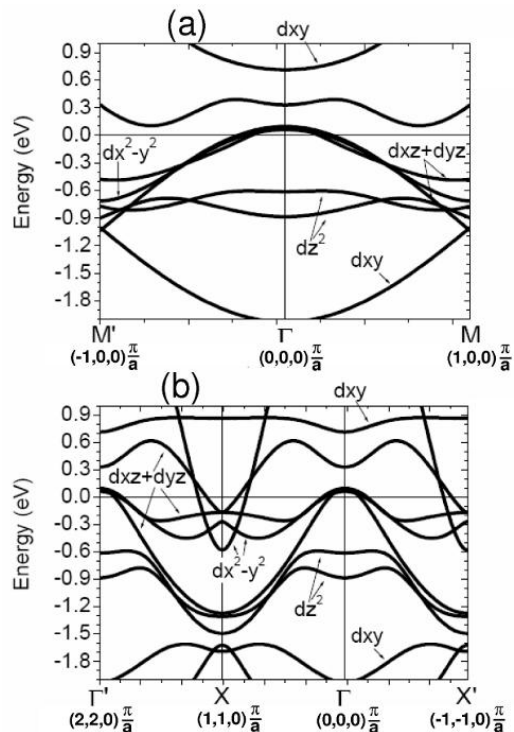


Figure 3: band structure calculation for tetragonal paramagnetic  $\text{BaFe}_2\text{As}_2$  for the energy region close to the Fermi level including an assignment of the dominant Fe 3d orbital character of the bands in the coordinate frame  $x = a$  and  $y = b$ . (a) The  $\Gamma$ -M direction. (b) The  $\Gamma$ -X direction.

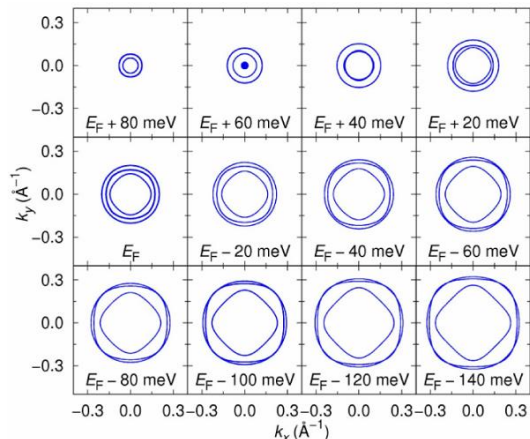


Figure 4: (color online) calculated constant energy contours for tetragonal paramagnetic  $\text{BaFe}_2\text{As}_2$  around the  $\Gamma$ -point for  $k_z=0$ .  $k_x$  is along the  $\Gamma$ -M direction.

wave vector  $k_F^y = 0.06 \pm 0.01 \text{ \AA}^{-1}$  and a Fermi velocity  $v_F^y = 0.85 \pm 0.04 \text{ eV \AA}$  along the  $k_y$  direction is estimated from the data shown in Fig. 6. Along the x-direction the Fermi wave vector is slightly larger ( $k_F^x = 0.11 \pm 0.01 \text{ \AA}^{-1}$ ). In Fig. 7 we show analogous data as in Fig. 6, but now taken with photons polarized along the horizontal direction, i.e., p-polarized radiation for a horizontal scat-

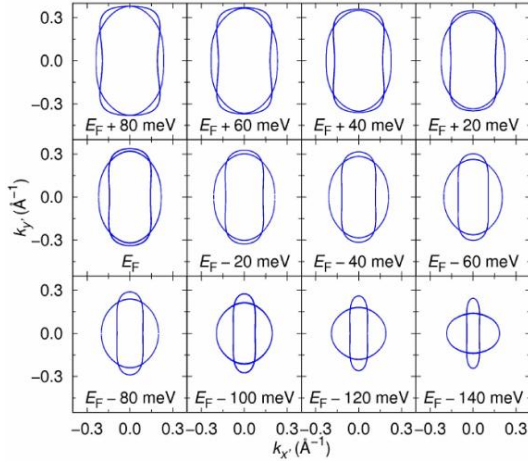


Figure 5: (color online) calculated constant energy contours for tetragonal paramagnetic BaFe<sub>2</sub>As<sub>2</sub> around the X-point for  $k_z=0$ .  $k_{x'}$  is along the  $\Gamma$ -X direction.

tering plane ( $k_y = 0$ ). The measurement temperature was  $T = 300$  K, well into the paramagnetic, tetragonal phase. Here, a circular Fermi surface is observed. The increasing size of the constant energy contours with increasing binding energy again indicates that at the  $\Gamma$ -point we have hole pockets. The Fermi wave vector and the Fermi velocity is  $k_F = 0.10 \pm 0.01 \text{ \AA}^{-1}$  and  $v_F = 0.72 \pm 0.05 \text{ eV\AA}$ , respectively. Contrary to the data taken with vertical photon polarization at  $E - E_F \approx -600$  meV spectral weight appears in the center of the zone. This indicates that there is now a band appearing which has a non-zero matrix element. Almost identical data were obtained at  $T = 20$  K (not shown), which gave  $k_F = 0.11 \pm 0.01 \text{ \AA}^{-1}$  and  $v_F = 0.72 \pm 0.05 \text{ eV\AA}$ . A remarkable result is that the Fermi surface, the Fermi wave vector, and the Fermi velocity do not change between  $T = 20$  K and  $T = 300$  K within error bars. In Fig. 8 we compare momentum distribution curves close to the Fermi level from a BFA100K crystal and from a BFA65K crystal recorded at  $T = 300$  K and  $T = 20$  K. In the BFA100K curve taken at low temperatures, clearly two hole pockets can be distinguished. This agrees with previous ARPES studies.<sup>6,9</sup> The corresponding Fermi wave vectors of the two bands are  $k_F = 0.10 \pm 0.01 \text{ \AA}^{-1}$  and  $k_F = 0.27 \pm 0.01 \text{ \AA}^{-1}$  and the corresponding Fermi velocities  $v_F = 0.69 \pm 0.06 \text{ eV\AA}$  and  $v_F = 0.75 \pm 0.05 \text{ eV\AA}$  are estimated along the  $k_y$  direction. At high temperatures it is more difficult to resolve the two bands due to the increased thermal broadening. Nevertheless  $k_F$  values for the two Fermi surfaces could be derived: for the inner and the outer Fermi surface we obtain  $k_F = 0.09 \pm 0.01 \text{ \AA}^{-1}$  and  $k_F = 0.28 \pm 0.01 \text{ \AA}^{-1}$ , respectively. The corresponding Fermi velocities are  $v_F = 0.72 \pm 0.08 \text{ eV\AA}$  and  $v_F = 0.73 \pm 0.06 \text{ eV\AA}$ , respectively. The curves from the BFA65K crystal are similar but slightly broadened possibly due to the higher Sn content which may lead to an additional scattering related to the impurity scattering. Therefore it is difficult to resolve contributions from the outer Fermi surface and

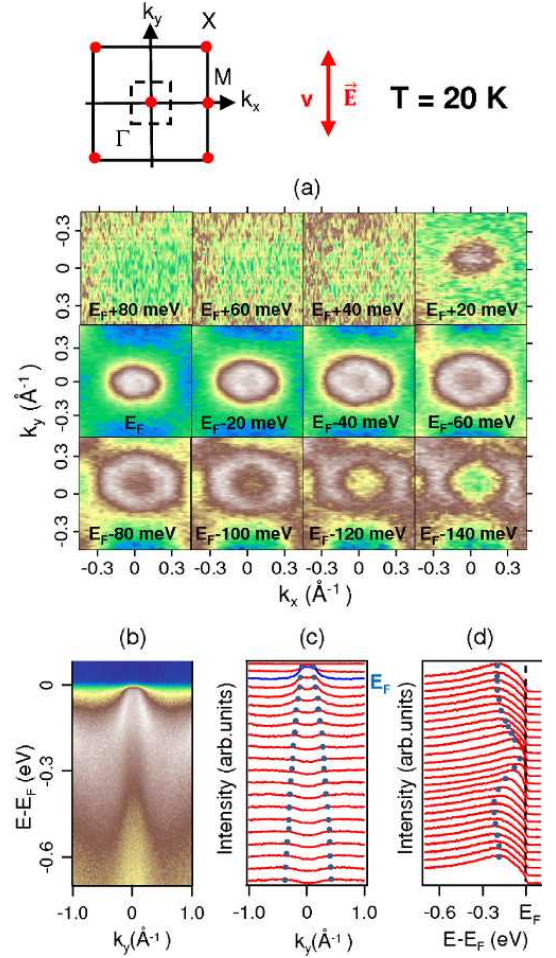


Figure 6: (color online) ARPES data around the center of the Brillouin zone ( $\Gamma$ -point) of BaFe<sub>2</sub>As<sub>2</sub> (BFA65K crystal) measured with a photon energy  $h\nu = 75$  eV. The top line shows the two-dimensional Brillouin zone together with the scanning range (dashed line). It also gives the polarization of the photons (in this case vertical and parallel to  $k_y$ ) and the recording temperature (here 20 K). (a) Momentum distribution maps for different binding energies derived by an integration over an energy range of 10 meV. (b) Spectral intensities as a function of  $k_y$  and binding energy for  $k_x = 0$ . (c) Momentum distribution curves for  $E - E_F = 50$  to  $-700$  meV. (d) Energy distribution curves for wave vectors parallel to  $k_y$  ranging from  $-1 \text{ \AA}^{-1}$  to  $1 \text{ \AA}^{-1}$ .

the Fermi wave vectors and the Fermi velocities for the BFA65K sample given above are mainly related to the inner Fermi surface.

In the following we present data taken near the X-point. Now the horizontal  $k_{x'}$  direction is parallel to  $\Gamma$ -X, i.e., the crystal has been rotated by  $45^\circ$  around the surface normal (see Section II). In Fig. 9 we show data taken at  $T = 20$  K with horizontal photon polarization. This means that in the center of the analyzer slit ( $k_{y'} = 0$ ) we have p-polarization. While close to the Fermi level there is more a circular spectral weight distribution, at lower energy ( $E - E_F < -60$  meV) an elongated

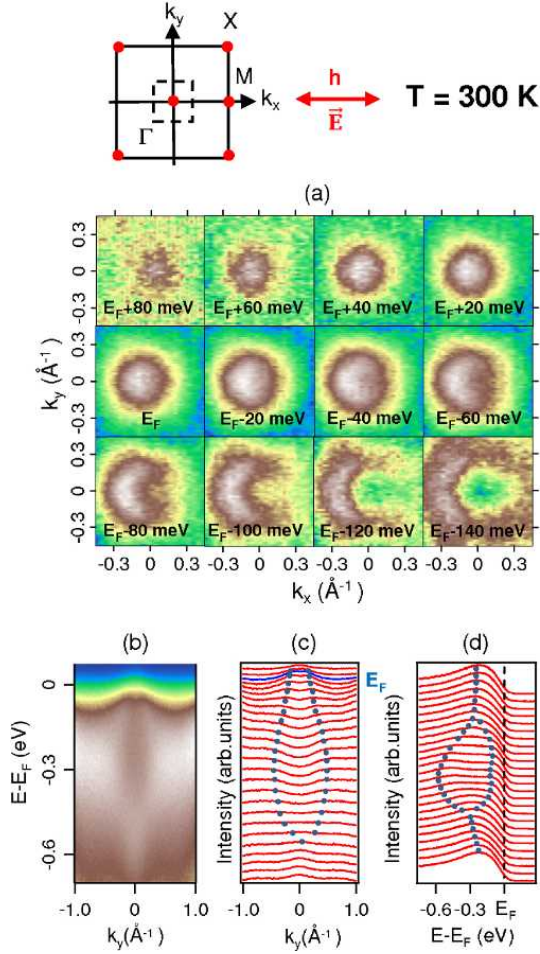


Figure 7: (color online) analogous data as in Fig. 6 but now recorded with a horizontal photon polarization (parallel to  $k_x$ ) and at a temperature  $T = 300$  K.

propeller-blade like distribution along the  $k_y$  direction is realized. In Fig. 10 we present analogous data but taken at  $T = 300$  K. Essentially the data are very close to the low temperature data. In similar spectra but now taken with vertical polarization at  $T = 20$  K, shown in Fig. 11, a circular Fermi surface with a Fermi wave vector  $k_F = 0.16 \pm 0.02 \text{ \AA}^{-1}$  is detected while at higher binding energies ( $E - E_F < -60$  meV) an elongated blade-like distribution along the  $k_x$  direction is visible (see Fig. 11). As will be outlined in Section V shortly, the differences between data recorded using the two polarizations can be attributed to matrix element effects (selection rules), which enable us to conclude about the orbital character of the states involved.

Finally, in Fig. 12 we present cuts along the  $\Gamma$ -N direction (parallel to  $k_y$ ) for various photon energies and normal photoelectron emission recorded from a BFA100K crystal at  $T = 20$  K. This data is very useful in the context of the comparison between the ARPES and DFT data, as *via* the identification of periodicities (vs. photon energy) we are able to cross-check our position in  $k_z$ , as in

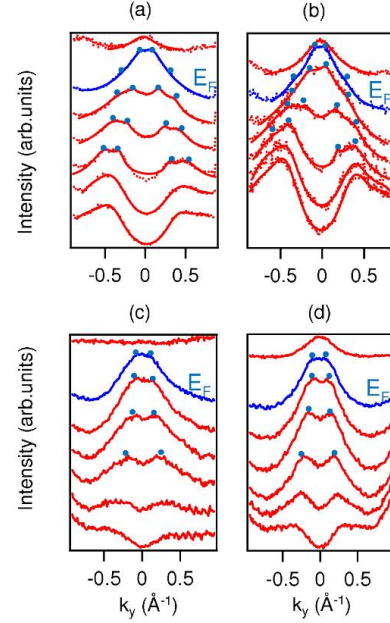


Figure 8: (color online) ARPES momentum distribution curves for  $E - E_F = 30$  to  $150$  meV near the  $\Gamma$ -point for  $k_x = 0$  along the  $k_y$  direction for a BFA100K and a BFA65K crystal using horizontally polarized photons with energies  $h\nu = 50$  eV and  $h\nu = 75$  eV, respectively. The solid lines are based on a fit to the data. A geometry was used as depicted in Fig. 7. (a) BFA100K crystal at  $T = 20$  K. (b) BFA100K crystal at  $T = 300$  K. (c) BFA65K crystal at  $T = 20$  K. (d) BFA65K crystal at  $T = 300$  K.

this measurement, the wave vector parallel to the FeAs layers is directed along the  $k_y$  direction and the  $k_z$  values are varied as the photon energy changes. The most clear result visible in Fig. 12 is that, near  $E - E_F = -600$  meV, a remarkable reduction of spectral weight is observed for the photon energies  $h\nu = 100$  and  $150$  eV. This effect will be discussed in Section V.

## V. DISCUSSION

First we discuss the results obtained near the  $\Gamma$ -point shown in Figs. 6 to 8. According to the present band structure calculations and those published in the literature<sup>17,18,19,20</sup> for the paramagnetic tetragonal state the in-plane Fermi surface at the  $\Gamma$ -point should be caused by three hole pockets formed by three bands which are almost degenerate (see e.g. Fig. 3(a) and the panel  $E_F$  in Fig. 4). The orbital character of the three bands at the  $\Gamma$  and at the Z-point is predicted to be related to mainly Fe  $3d_{x^2-y^2}$ , Fe  $3d_{yz}$ , and Fe  $3d_{xz}$  states. In the calculations, these bands show dispersion along the  $\Gamma$ -Z direction which leads to a departure from a simple cylindrical form of the Fermi surface as a function of  $k_z$  value. For  $k_z = 0$  the Fermi wave vectors for the Fe  $3d_{x^2-y^2}$ , Fe  $3d_{xz}$ , and Fe  $3d_{yz}$  bands are  $0.17$ ,  $0.14$ , and  $0.20 \text{ \AA}^{-1}$ , respectively. For a  $k_z$  value at the zone

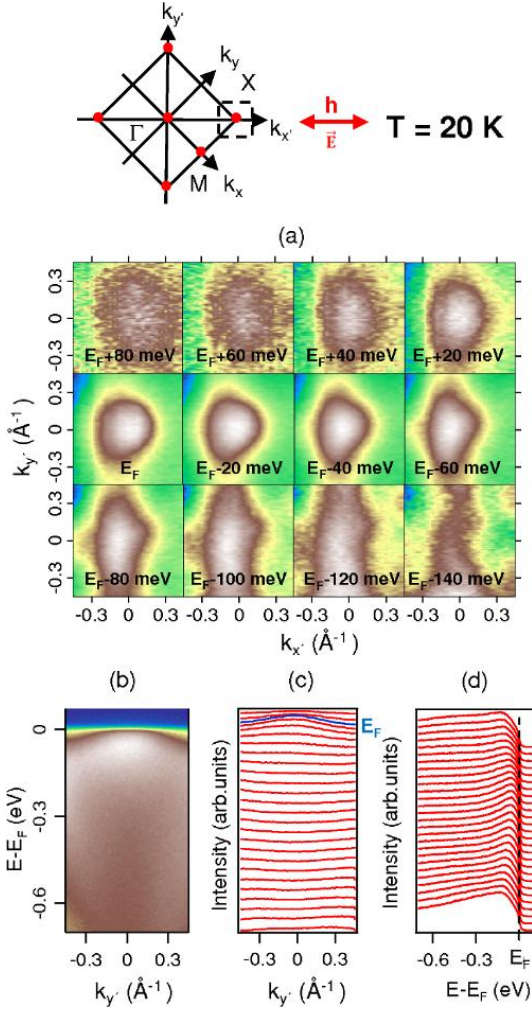


Figure 9: (color online) similar data as in Fig. 7 measured with a photon energy  $h\nu = 75$  eV but now around the X-point and at a temperature was  $T = 20$  K. Horizontal photon polarization (parallel to  $k_{x'}$ ) has been used. The horizontal  $k_{x'}$  direction is aligned parallel to the  $\Gamma$ -X direction.

boundary, the splitting between the three bands is increased and essentially two larger Fermi surfaces with  $k_F$  values of 0.22 and 0.42  $\text{\AA}^{-1}$  are predicted. At the  $\Gamma$ -point two further bands with mainly Fe  $3d_{z^2}$  character appear near  $E - E_F = -600$  and  $-900$  meV. For  $k_z$ -values between the  $\Gamma$  and the Z-point these bands disperse toward the Fermi level and reach an energy of  $\approx -100$  meV.

As described in Section II, due to matrix element effects for horizontal (vertical) polarization of the incoming photons and a horizontal scattering plane, odd(even) initial states relative to the  $\Gamma$ MZ mirror plane should disappear. For the data shown in Fig. 6, where the photons were polarized vertically (s-polarization), all even states relative to the mirror plane, i.e., Fe  $3d_{x^2-y^2}$ , Fe  $3d_{z^2}$ , and Fe  $3d_{xz}$ , should disappear along the horizontal  $k_y = 0$  line, but the other two odd Fe  $3d$  orbitals (Fe  $3d_{xy}$  and Fe  $3d_{yz}$ ) should contribute to the spectral weight along this line. Since the Fe  $3d_{xy}$  bands are outside the en-

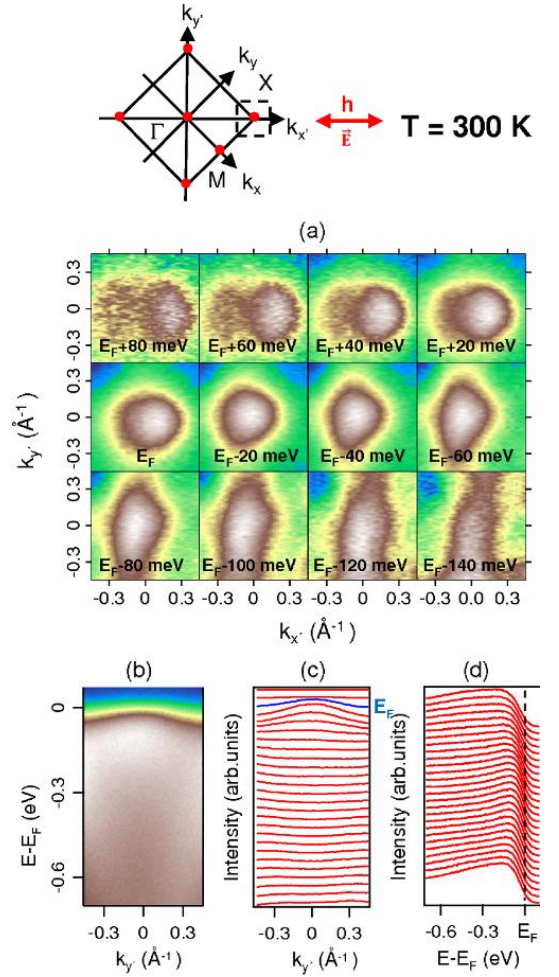


Figure 10: (color online) similar data as in Fig. 9 around the X-point but now with the recording temperature  $T = 300$  K. Again a horizontal photon polarization has been used.

ergy range presented in these measurements only the Fe  $3d_{yz}$  band contributes along the horizontal  $k_y = 0$  line. For data taken with horizontal photon polarization (p-polarization, presented in Fig. 7), and for a cut through the data with  $k_y = 0$ , the odd Fe  $3d_{yz}$  (and  $3d_{xy}$ ) states should be suppressed, but all other Fe  $3d$  bands near the Fermi should be visible.

As pointed out before in all data taken at the center of the two-dimensional Brillouin zone (see Figs. 6 to 8), one clearly sees one or two hole pockets, i.e., Fermi surfaces in the  $k_x, k_y$  plane, the diameter of which decreases when going from below to above the Fermi level. It is remarkable that the diamond-like constant energy contour predicted in Fig. 4 for the Fe  $3d_{x^2-y^2}$  states at higher binding energies is well reproduced in the experimental data.

In the following we attempt a more quantitative comparison of the ARPES data near the Fermi energy with the band structure calculations. We warn the reader in advance that a fully self-consistent assignment that matches the data one-on-one with the LDA bands is not

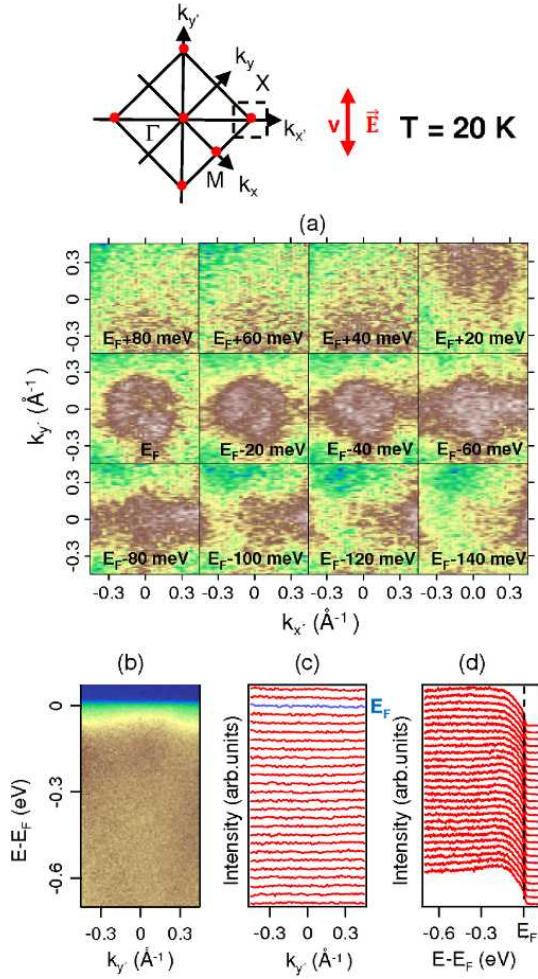


Figure 11: (color online) similar data as in Fig. 9 taken at a temperature of 20 K but with vertical photon polarization (parallel to  $k_y$ ).

achievable: most probably a result of the multiband nature of these materials, the uncertainty experimentally about the exact value of  $k_z$  and the fact that knowledge about the  $k$ ,  $E$  and polarization dependence of the photoionisation matrix elements in these systems is only just starting to be gathered.

Since in the data shown in Fig. 6 near the  $k_y = 0$  line we should only see Fe  $3d_{yz}$  states near the Fermi surface, the experimental value  $k_F^y = 0.11 \pm 0.01 \text{ \AA}^{-1}$  should be compared with the theoretical value  $k_F = 0.20 \text{ \AA}^{-1}$  for the Fe  $3d_{yz}$ -derived hole pocket. For the  $k_y$  direction we should observe the same value as along the  $k_x$  direction, but in the experiment a considerably smaller value  $k_F^y = 0.06 \pm 0.01 \text{ \AA}^{-1}$  is observed. An explanation for this reduced Fermi wave vector along the  $k_y$  direction could be that moving to non-zero  $k_y$  values, also spectral weight should appear from one or both of the two low energy even-symmetry bands formed by overlap between the Fe  $3d_{xz}$  and Fe  $3d_{x^2-y^2}$  states. Assuming smaller  $k_F$  values for one or both of these even symmetry bands could result

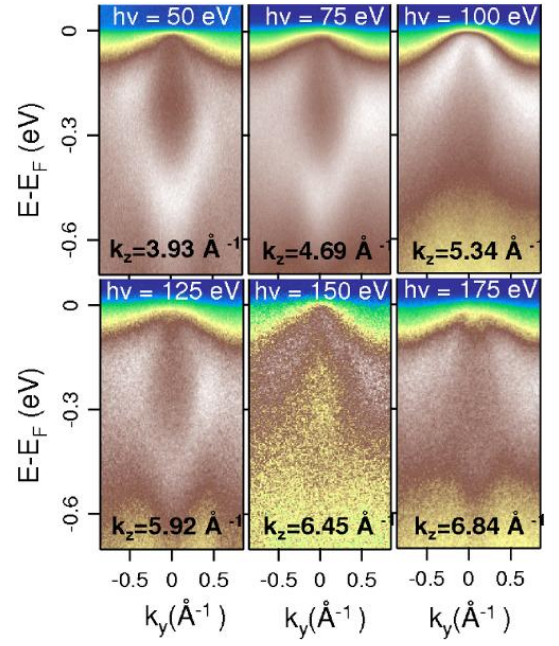


Figure 12: (color online). ARPES data from a BFA100K crystal recorded around the center of the Brillouin zone ( $\Gamma$ -point) measured with horizontal photon polarization and variable photon energies ranging from  $h\nu = 50$  to 175 eV. Data are recorded in normal emission at a temperature of  $T = 20$  K.  $k_x$  is parallel to the  $\Gamma$ -M direction.

in an apparent asymmetric Fermi surface with a smaller diameter along the  $k_y$  direction. With a view to the band structure data for  $k_z=0$ , we tentatively assign the Fermi surface with the small  $k_F^y$  value to the Fe  $3d_{x^2-y^2}$ -related states.

In the data recorded with horizontally polarized light shown in Figs. 7 and 8, the outer Fermi surface with  $k_F = 0.27 \pm 0.01 \text{ \AA}^{-1}$  can be tentatively assigned to the Fe  $3d_{xz}$  states. In this way we can arrive at qualitative but not quantitative agreement with the band structure calculations, assuming our ARPES data with 75eV photons to be representative for  $k_z=0$  (we will present arguments as to why we believe this to be the case later on). The experimental  $k_F$  values are somewhat different from the calculated ones and the experimentally observed splitting of the three bands is about a factor three larger than the calculated one. For the spectra taken with horizontal photon polarization (see Fig. 7), the experimental Fermi surface near the  $k_y = 0$  line should be caused by the even Fe  $3d_{x^2-y^2}$  and Fe  $3d_{xz}$  bands. Thus, based on the assignment made above, a small Fermi wave vector of ca.  $k_F = 0.06 \text{ \AA}^{-1}$  is expected here too (the Fe  $3d_{x^2-y^2}$  band), yet in these data we find experimentally a value of  $k_F = 0.11 \pm 0.01 \text{ \AA}^{-1}$ . The observation of an even larger second Fermi surface in the data shown in Fig. 8 with a Fermi vector  $k_F = 0.27 \pm 0.01 \text{ \AA}^{-1}$  which consequently would need to be assigned to the Fe  $3d_{xz}$  bands, a fact which would not match with the interpretation we proposed for the asymmetric Fermi surface detected for

vertical photon polarization shown in Fig. 6. This discussion serves to illustrate that further work is necessary to obtain an unambiguous assignment of the detected bands to the results of DFT band structure calculations.

Taking the lack of one-to-one quantitative agreement between the ARPES data and the band structure calculations at face value, we now mention and comment on the following possible origins for these differences - at least for the states close to  $E_F$ . (i) The surface doping level and/or electronic structure is different to that for the bulk. This could be due to the formation of polar surfaces connected with a small shift of the chemical potential, or due to reconstructions following on from the significant disorder seen in the Ba termination layer of these crystals using STM,<sup>7,31,32</sup> which could then change the electronic structure of the FeAs block closest to the surface. A further source of a surface/bulk difference could be a relaxation of the As-Fe-As distances at the surface, as we know from our DFT calculations that the electronic structure of these compounds is very sensitive to the Fe-As distance. However, a scenario involving a different surface electronic structure compared to the bulk is constrained by a recent high-energy, angle-integrated photoemission spectroscopic study conducted by some of us on BaFe<sub>2</sub>As<sub>2</sub>, which concludes that there are, at most, minor alterations of the electronic structure at the surface compared to the bulk.<sup>22</sup> (ii) A second scenario would involve the existence of a large in-plane antiferromagnetic correlation length in the paramagnetic state of BaFe<sub>2</sub>As<sub>2</sub> which may shift the electronic states with respect to the purely paramagnetic state assumed in the calculations, and would also provide a basis for the essential lack of temperature dependence seen in the experimental data. (iii) Thirdly, from the experimental point of view, we have an uncertainty in the  $k_z$  values. This scenario suffers from the drawback that the diameter of our largest  $\Gamma$ -centered Fermi surface is smaller (by a factor of almost one half) than the maximal DFT-predicted value at the Z-point: thus even allowing ourselves a totally free choice of our true  $k_z$ -value in experiment, there still remain discrepancies between the ARPES and DFT data. In addition to this point, we present arguments below in favor of the fact that we know the  $k_z$ -location of the data recorded with the photon energies 50 and 75 eV to be close to zero (i.e. at the  $\Gamma$ -point).

Next we discuss the Fermi velocities derived for the Fermi surfaces near the  $\Gamma$ -point. From the band structure calculations we obtain values between 0.7 and 1.1 eVÅ for the three bands along the  $\Gamma$ -M direction. This is in fair agreement with the experimental values  $v_F \approx 0.8$  eVÅ along the same direction determined from spectra taken for vertical and horizontal photon polarization. Thus the present measurements do not indicate a large mass renormalization of the bands near the  $\Gamma$ -point. On the other hand, with the present energy resolution we cannot exclude a mass renormalization due to bosonic excitations with an energy less than  $\approx 20$  meV, since the bands should be renormalized only below the energy of

the bosonic excitations.

At higher binding energies we obtain nice agreement between the band structure calculations and the experimental data presented in Figs. 6 and 7. The Fe  $3d_{z^2}$  band, which according to Fig. 3 should appear near an  $E - E_F$  value of -600 meV, is clearly visible in the data taken with horizontal polarization shown in Fig. 7(b), which is consistent with the orbital origin of these states which is always even with respect to the  $\Gamma$ MZ mirror plane. On the other hand for vertical photon polarization, these states should disappear, which is indeed exactly what they do, as can be seen from the data shown in Fig. 6(b). The fact that such an unambiguous assignment of these 600meV states for the p-polarisation geometry is possible, presents us with a clear and thus powerful 'tool' to gauge the position of our ARPES data with respect to the relevant value of  $k_z$ . As mentioned earlier, for  $k_z=0$ , these states should lie at ca. 600meV. They are predicted (within DFT) to disperse up to only within 100 meV of  $E_F$  for  $k_z$  values at the bottom or top of the Brillouin zone. This means, therefore, that the observed binding energy (600meV) of these Fe  $3d_{z^2}$  states for  $k_x=k_y=0$  thus 'pins' the data recorded using 75eV photons to  $k_z$  values at or close to zero.

At the end of the discussion of the data at  $\Gamma$ (Z) we point out that we did not observe a significant change of the electronic structure when going from the tetragonal paramagnetic phase at high temperatures to the orthorhombic antiferromagnetic phase at low temperatures. This observation is in line with previous ARPES studies<sup>6</sup> but not with previous spin polarized DFT band structure calculations<sup>21,30</sup> which predicted a large change of the electronic structure near the  $\Gamma$ -point in the orthorhombic antiferromagnetic phase. On the one hand, this difference could possibly be attributed to the strong itineracy of the BaFe<sub>2</sub>As<sub>2</sub> system which causes only small changes of the electronic structure, while spin polarized DFT calculations overestimate the magnetic moment and thus predicting large changes of the electronic structure. On the other hand, as alluded to earlier, there also exists the possibility that even above  $T_N$  strong quasi-2D antiferromagnetic spin-spin correlations (of reasonably long range) are to be found within the FeAs layers. This would mean that the two-dimensional electronic structure within these layers is only very weakly altered when crossing the bulk, three-dimensional spin-ordering temperature,  $T_N$ .

In the following we discuss the results around the X-point. According to the band structure calculations (see Figs. 3 and 5) the in-plane Fermi surfaces around this high-symmetry point should be caused by two electron pockets. The larger one is mainly formed by Fe  $3d_{x^2-y^2}$  states while the smaller one has mainly Fe  $3d_{xz}$  and Fe  $3d_{yz}$  character. Measuring from X towards the  $\Gamma$ -point, the  $k_F$  values are predicted to be 0.14 and 0.22 Å<sup>-1</sup>. The band-bottoms of the small and the large electron pockets are predicted by DFT to appear at  $E - E_F = -180$  meV and -550 meV, respectively. At -180 meV, a third

weakly dispersing band appears in the calculations which has mainly Fe  $3d_{xz}$  and Fe  $3d_{yz}$  character. A further band with a larger dispersion having mainly Fe  $3d_{x^2-y^2}$  character is predicted at around -300 meV.

In all data taken near the X-point, the crystal was oriented in such a way that a  $\Gamma XZ$  mirror plane is in the scattering plane for the center of the exit slit of the analyser ( $k_{y'} = 0$ ). In the data for vertical (i.e. s) polarization shown in Fig. 11, an almost spherical Fermi surface is detected around the X-point, with a Fermi vector  $k_F = 0.16 \pm 0.02 \text{ \AA}^{-1}$ . For this photon polarization, the experimentally observed Fermi surface could be related to all three bands close to the Fermi level having Fe  $3d_{yz}$ , Fe  $3d_{xz}$ , and Fe  $3d_{x^2-y^2}$  character. The experimental  $k_F$  value is not far from that predicted from the band-structure calculations for the smaller (Fe  $3d_{yz}$ , Fe  $3d_{xz}$ ) electron pocket.

According to the calculations presented in Fig. 5, with increasing binding energy the constant energy surfaces around the X-point should change shape quite significantly. The elliptical energy surface (with its long axis pointing along  $k_{y'}$ ) increases in aspect ratio significantly as the binding energy increases, until these states finally disappear near -180 meV. The second Fermi surface seen in Fig. 5 is due to the Fe  $3d_{x^2-y^2}$  states, and transforms with increasing binding energy from an ellipse with its long axis pointing along  $k_{y'}$  at  $E_F$  to a more rounded form, slightly elongated along  $k_{x'}$  at higher binding energies. According to the DFT data, the band-bottom for these states should lie at an  $E - E_F$  of ca. -600 meV, with another (quite flat) band of the same symmetry bottoming out at roughly half this value.

The experimental results shown in Fig. 11(a), although hampered by the low cross-section for these conditions, show a small, rounded Fermi surface, transforming into a blade-like intensity distribution with its long axis along  $k_{x'}$ , before the intensity essentially runs out at -140 meV. Given the s-polarisation used to record this data, we would expect to be sensitive to the Fe  $3d_{x^2-y^2}$  states along the  $k_{y'} = 0$  line, thus the fact that the constant energy cuts broaden parallel to  $k_{x'}$  with increasing binding energy is an aspect that matches with the DFT predictions. It is less clear at present why the observed intensity for  $E = E_F$  is essentially 'round', and not elongated along  $k_{y'}$  as along this direction one leaves the relevant mirror plane and thereby relaxes the symmetry selection rules that form part of the matrix elements. The same goes for the fact that we do not see a sign of the deeper lying Fe  $3d_{x^2-y^2}$  states in either Fig. 11(b) or (d), although we do remark that the scattering rates at these energies are possibly already rather high and thus these bands cannot be resolved from the incoherent background, which may be substantial due to the Sn impurity scattering.

For the analogous data taken with horizontal (i.e. p) polarization, shown in Figs. 9 and 10, the odd Fe  $3d_{x^2-y^2}$  states should disappear near the  $k_{y'} = 0$  line but the Fe  $3d_{xz}$  and Fe  $3d_{yz}$  states should remain visible. In both figures, the higher binding energy intensity distribution

now no longer takes on the form of a blade-like structure parallel to  $k_{x'}$ , but rather one parallel to  $k_{y'}$ , as would be expected for the Fe  $3d_{xz}$  and Fe  $3d_{yz}$  states upon inspection of Fig. 5. For the data at  $E_F$ , the fact that the high intensity seems more concentrated close to  $k_{x'}=k_{y'}=0$  with respect to the data of Fig. 11(a) would offer support for the DFT prediction of a narrower Fermi surface cross-section parallel to  $k_{x'}$  for the Fe  $3d_{xz}$  and Fe  $3d_{yz}$  related states. It remains a moot point whether the low temperature data for energies at or close to  $E_F$  show signs of an elliptical intensity distribution with its long axis along  $k_{y'}$  or not. In any case, what is highly evident from both the low temperature (Fig. 9) and room temperature (Fig. 10) data from the X-point is that the intensity for positive  $E - E_F$  values is much more robust, being clearly visible - even for the 20K data - up to energies some 80 meV above  $E_F$ . This is in stark contrast to the data of Fig. 6, taken around the  $\Gamma$ -point, whereby already only 40 meV above  $E_F$  all intensity has disappeared. These facts serve as a clear indication of the electron-pocket nature of the states near X, and at the same time of the fact that the top of the band forming the hole pocket at  $\Gamma$  is not far above the Fermi level in these samples.

It is interesting to note that even for temperatures well below the transition temperature from the tetragonal paramagnetic state to the orthorhombic antiferromagnetic state, we see clear Fermi surfaces in Figs. 9 to 11, which would indicate that there is no massive gapping of the Fermi surface going on, due to a nesting between the Fermi surfaces at the  $\Gamma$  and the X-point. If such a gapping exists, we are not able to resolve it in the present data. These results are again in agreement with previous ARPES studies<sup>6</sup> on  $\text{BaFe}_2\text{As}_2$ . On the other hand the present results are at variance with ARPES data<sup>15</sup> measured on paramagnetic, K-doped  $\text{BaFe}_2\text{As}_2$  in which a splitting of the bands at the X-point due to nesting was proposed.

At the end of this Section we discuss the photon energy dependent data recorded around the  $\Gamma$ -point, shown in Fig. 12. The clearest conclusions from these data involve the clear presence or absence of spectral weight with a band-bottom at  $E - E_F = -600\text{meV}$ . As discussed earlier in the light of our exploitation of the symmetry selection rules valid for the use of linear vertical and linear horizontal synchrotron radiation, these states have mainly Fe  $3d_{z^2}$  character. All data in Fig. 12 are recorded with p-polarised light, so the mirror symmetry of these states means that they can be detected. For the panels of Fig. 12 taken with photon energies of 50, 75, 125 and to a slightly lesser extent 175 eV, these Fe  $3d_{z^2}$  states are clearly seen with a binding energy of some 600 meV for  $k_y=0$ . This binding energy value is, in itself, a clear sign that, for these photon energies, we are probing states with  $k_z=0$ , i.e., we are probing the  $\Gamma$ -point or symmetry-equivalent points in higher Brillouin zones. For the photon energies of 100 and 150 eV, the Fe  $3d_{z^2}$  states at 600meV are missing, indicating that their binding energy

is very different (a  $k_z$ -dependence of the energy of a band built up of out-of-plane  $3d_{z^2}$  states is not unreasonable) either/or there are strong matrix element differences sensitive to the  $k_z$  value that prohibit their detection. If we take a value of 13 eV for the inner potential (a value derived from the bottom of the valence band, taken from the data from the band structure calculations), we come to the  $k_z$  values shown in Fig. 12. For an effective period along the  $z$ -direction corresponding to the distance between two FeAs layers ( $c' = c/2$ ), the panels for  $h\nu = 50, 75, 125$ , and  $175$  eV would then correspond to  $k_z$  values close to zero (or even multiples of  $\pi/c'$ ), while the panels for  $h\nu = 100$  and  $150$  eV would correspond to  $k_z$  values close to  $\pi/c'$  or odd multiples thereof. This would place the latter two data sets close to the  $Z$ -point (see Fig. 1).

In this manner, the analysis of the data of Fig. 12 underpins our earlier discussion, in which we compared the  $k_z=0$  DFT band structure and constant energy surfaces (in Figs. 3, 4 and 5) with the ARPES data recorded with 75 eV photons. Furthermore, the  $k_z$  assignment made possible by the data of Fig. 12, combined with the inspection of the data themselves near  $E_F$  and  $k_y=0$  make it clear that the fairly 'closed' nature of the observed hole pocket near  $\Gamma$  indicates that it comes from the innermost Fermi surface predicted by DFT. The fact that the data panels in Fig. 12 recorded with photon energies of 100 and 150 eV do not show a grossly different 'open' or 'closed' nature of this hole pocket is not inconsistent with the fact that the DFT calculations for the innermost surface predict only a 40% variation in  $k_F$  between  $\Gamma$  and  $Z$ , compared to a 210% increase in  $k_F$  for the outermost  $\Gamma$ -centered hole pocket between  $\Gamma$  and  $Z$ .

Finally, despite some variation in the exact values of the photon energies used, we nevertheless note that the  $k_z$  assignments for the  $h\nu = 50$  and  $75$  eV data as being close to  $\Gamma$ , match reasonably with other ARPES results regarding the locations of the  $\Gamma$  and  $Z$ -points as a function of photon energy.<sup>16</sup>

## VI. CONCLUSIONS

In this ARPES study we have determined the electronic structure of  $\text{BaFe}_2\text{As}_2$ , a parent compound of

doped FeAs-based high- $T_c$  superconductors. The hole (electron) pocket nature of the frontier electronic states at  $\Gamma(X)$  has been confirmed. Experimental information has been derived both for the paramagnetic tetragonal state and the antiferromagnetic orthorhombic state. No significant changes could be resolved between the two phases, indicating that the real differences for the electronic structure between these two phases are probably much smaller than those predicted by spin-dependent DFT band structure calculations, a fact that supports a more itinerant character for the Fe 3d conduction electrons. In general, reasonable qualitative agreement between the band structure calculations for the paramagnetic state and the ARPES data has been observed, although in a number of points a direct assignment of the experimental photoemission intensity distributions to individual bands/Fermi surfaces is not without a residual level of ambiguity. Photon energy dependent measurements have enabled a clear identification of which photon energies (for experiments around normal emission) give access to  $k_z$  values at or near to the center of the Brillouin zone ( $\Gamma$ ) and which probe closer to the zone boundary in  $k_z$  ( $Z$ ). The same data suggest modest three-dimensionality for the innermost Fermi surface (with respect to the  $\Gamma Z$  line), which is in keeping with the DFT predictions.

## ACKNOWLEDGMENTS

Financial support by the DFG is appreciated by J.F. (Forschergruppe FOR 538) and by R.V. and H.O.J. (SFB/TRR49, Emmy Noether program). This work is part of the research programme of the 'Stichting voor Fundamenteel Onderzoek der Materie (FOM)', which is financially supported by the 'Nederlandse Organisatie voor Wetenschappelijk Onderzoek (NWO)'.

- 
- <sup>1</sup> Y. Kamihara, T. Watanabe, M. Hirano, and H. Hosono, *J. Am. Chem. Soc.* **130**, 3296 (2008).
  - <sup>2</sup> X. H. Chen, T. Wu, G. Wu, R. H. Liu, H. Chen, and D. F. Fang, *Nature (London)* **453**, 761 (2008).
  - <sup>3</sup> H. Takahashi, K. Igawa, K. Arii, Y. Kamihara, M. Hirano, and H. Hosono, *Nature (London)* **453**, 376 (2008).
  - <sup>4</sup> M. Rotter, M. Tegel, and D. Johrendt, *Phys. Rev. Lett.* **101**, 107006 (2008).
  - <sup>5</sup> I. I. Mazin, D. J. Singh, M. D. Johannes, and M. H. Du, *Phys. Rev. Lett.* **101**, 057003 (2008).
  - <sup>6</sup> L. Yang, Y. Zhang, H. Ou, J. Zhao, D. Shen, B. Zhou,

- J. Wei, F. Chen, M. Xu, C. He, et al., arXiv:0806.2627 (2008).
- <sup>7</sup> D. Hsieh, Y. Xia, L. Wray, D. Qian, K. Gomes, A. Yazdani, G. Chen, J. Luo, N. Wang, and M. Hasan, arXiv:0812.2289v1 (2008).
- <sup>8</sup> M. Yi, D. H. Lu, J. G. Analytis, J.-H. Chu, S.-K. Mo, R.-H. He, X. J. Zhou, G. F. Chen, J. L. Luo, N. L. Wang, et al., arXiv:0902.2628v1 (2009).
- <sup>9</sup> C. Liu, G. D. Samolyuk, Y. Lee, N. Ni, T. Kondo, A. F. Santander-Syro, S. L. Bud'ko, J. L. McChesney, E. Rotenberg, T. Valla, et al., *Phys. Rev. Lett.* **101**, 177005 (2008).

- <sup>10</sup> H. Ding, P. Richard, K. Nakayama, K. Sugawara, T. Arakane, Y. Sekiba, A. Takayama, S. Souma, T. Sato, T. Takahashi, et al., EPL **83**, 47001 (2008).
- <sup>11</sup> P. Richard, T. Sato, K. Nakayama, S. Souma, T. Takahashi, Y.-M. Xu, G. Chen, J. Luo, N. Wang, and H. Ding, arXiv:0808.1809 (2008).
- <sup>12</sup> L. Wray, D. Qian, D. Hsieh, Y. Xia, and L. Li, Phys. Rev. B **78**, 184508 (2008).
- <sup>13</sup> D. Evtushinsky, D. Inosov, V. Zabolotnyy, A. Koitzsch, M. Knupfer, B. Buechner, G. Sun, V. Hinkov, A. Boris, C. Lin, et al., arXiv:0809.4455 (2008).
- <sup>14</sup> H. Liu, W. Zhang, L. Zhao, X. Jia, J. Meng, G. Liu, X. Dong, G. Chen, J. Luo, N. Wang, et al., Phys. Rev. B **78**, 184514 (2008).
- <sup>15</sup> V. Zabolotnyy, D. Inosov, B. Evtushinski, A. Koitzsch, A. Kordyuk, J. Park, D. Haug, V. Hinkov, A. Boris, G. Sun, et al., Nature **457**, 569 (2009).
- <sup>16</sup> P. Vilmercati, A. Federov, I. Vobornik, U. Manju, G. Panaccione, A. Goldoni, A. Sefat, M. McGuire, B. Sales, R. Jin, et al., arXiv:0902.0756 (2009).
- <sup>17</sup> D. J. Singh, Phys. Rev. B **78** (2008).
- <sup>18</sup> I. R. Shein and A. L. Ivanovskii, JETP Lett. **88**, 107 (2008).
- <sup>19</sup> I. A. Nekrasov, Z. V. Pchelkina, and M. V. Sadovskii, JETP Lett. **88**, 144 (2008).
- <sup>20</sup> J. Shim, K. Haule, and G. Kotliar, Phys. Rev. B **79**, 060501 (2009).
- <sup>21</sup> F. Ma, Z. Lu, and T. Xiang, arXiv:0806.3526 (2008).
- <sup>22</sup> S. de Jong, Y. Huang, R. Huisman, F. Massee, S. Thirupathiah, M. Gorgoi, R. Follath, J. B. Goedkoop, and M. S. Golden, arXiv.org:0901.2691 (2009).
- <sup>23</sup> N. Ni, S. Bud'ko, A. Kreyssig, S. Nandi, G. Rustan, A. Goldman, S. Gupta, J. Corbett, A. Kracher, and P. Canfield, arXiv:0806.1874 (2008).
- <sup>24</sup> Y. Su, P. Link, A. Schneidewind, T. Wolf, Y. Xiao, R. Mittal, M. Rotter, D. Johrendt, T. Brueckel, and M. Loewenhaupt, arXiv 0807.1743 (2008).
- <sup>25</sup> D. S. Inosov, R. Schuster, A. A. Kordyuk, J. Fink, S. V. Borisenko, V. B. Zabolotnyy, D. V. Evtushinsky, M. Knupfer, B. Buechner, R. Follath, et al., Phys. Rev. B **77** (2008).
- <sup>26</sup> S. Huefner, *Photoelectron Spectroscopy* (Springer Verlag, Berlin and Heidelberg, 1994).
- <sup>27</sup> J. Perdew, S. Burke, and M. Ernzerhof, Phys. Rev. Lett. **77**, 3865 (1996).
- <sup>28</sup> P. Blaha, K. Schwarz, G. K. Madsen, D. Kvasnicka, and J. Luitz, *WIEN2k, An Augmented Plane Wave + Local Orbitals Program for Calculating Crystal Properties* (K. Schwarz, Technical University Wien, Wien, Austria, 2001).
- <sup>29</sup> Q. Huang, Y. Qiu, W. Bao, M. A. Green, J. W. Lynn, Y. C. Gasparovic, T. Wu, G. Wu, and X. H. Chen, Phys. Rev. Lett. **101**, 257003 (2008).
- <sup>30</sup> Y.-Z. Zhang, H. C. Kandpal, I. Opahle, H. O. Jeschke, and R. Valenti, arXiv:0812.2920 (2008).
- <sup>31</sup> Y. Yin, M. Zech, T. L. Williams, X. F. Wang, G. Wu, X. H. Chen, and J. E. Hoffman, arXiv:0810.1048 (2008).
- <sup>32</sup> F. Massee, Y. Huang, R. Huisman, S. de Jong, J. B. Goedkoop, and M. S. Golden, arXiv:0812.4539 (2008).